Journal of the Ceramic Society of Japan 121 [2] 142-149 2013 Special Article
The 66th CerSJ Awards for Advancements in Ceramic Science and Technology: Review

Synthesis, structure and properties of new functional oxynitride ceramics

Yuji MASUBUCHI†

Faculty of Engineering, Hokkaido University, N13 W8, Kita-ku, Sapporo 060–8628, Japan

Novel metal oxynitrtides have been prepared by nitridation of amorphous metal oxide precursors obtained through citrate route. Their crystal structure, especially in O/N distribution and local bonding characteristics has been analyzed by using neutron diffraction, X-ray absorption and transmission electron microscopy, to investigate their electric and optical properties. In dielectric $SrTaO_2N$, crystal structure refinement suggested the short range O/N ordering and local tilting of *cis*-TaO_4N_2 octahedra, resulting in its unusual large permittivity. Its dense ceramics were sintered with $SrCO_3$ additive and exhibited superior dielectric constant above 1×10^4 at room temperature. New biphasic wurtzite and zinc-blende structure of gallium oxynitride nanowire was observed by using transmission electron microscopy. As-grown long gallium oxynitride nanowire exhibited a characteristic broad UV emission at 4.3 eV in its cathodoluminescene spectrum. New oxynitride phosphor having magneto-plumbite structure, $LaAl_{12}(O,N)_{19}$:Eu showed photoluminescence emission peak splitting due to Eu^{2+} site splitting to two crystallographic sites induced by the two kinds of anions in its crystal structure.

Key-words : Oxynitrides, Crystal structure, Neutron diffraction, Dielectric property, Optical properties

[Received October 1, 2012; Accepted November 13, 2012]

1. Introduction

Oxynitrides are a novel group of compounds attracting recent interest for new applications and scientific investigation. Many kinds of oxynitrides have been prepared in the last decades and their applications are also developing. Their chemistry has been widely reviewed and their properties have been explained by the nitride ion coexisting with oxide ion in their crystal lattice.[1)–3)] The nitride ion has a lower electronegativity than oxide ion ($\chi_O = 3.50 > \chi_N = 3.05$) and they have different charge. The substitution of O^{2-} with N^{3-} induces the cross-substitution of M^{2+} with M'^{3+} or formation of anion vacancy, in order to keep charge neutrality.[4)] Such oxynitrides have also been studied in applications such as phosphor materials,[5),6)] visible light photocatalysis,[7),8)] inorganic non-toxic pigment,[9),10)] gas sensor,[11)] and dielectric materials.[12)–16)] However, the kinds of oxynitrides are still very limited as compared with those of oxides.

Oxynitride phosphor materials have been widely studied in silicon (oxy)nitride and alumino-silicon (oxy)nitrides host materials such as α- and β-SiAlONs,[1),2),17)] spinel type AlON[18)] and $CaAlSiN_3$.[19)] Such (oxy)nitrides have been prepared by high temperature solid state reaction using starting powder mixtures of oxides and nitrides under compressed nitrogen atmosphere. On the other hand, multinary oxynitrides consisting of transition metals and alkali, alkali earth or lanthanum metals have been obtained through high temperature nitridation of crystalline precursors under an ammonia flowing.[20)–22)] Multinary oxides or mixture of oxides/carbonates were generally used as the precursors. The thermal ammonolysis was successfully applied to obtain several kinds of oxynitrides, while the reaction has some disadvantages. The ammonolysis reaction requires the diffusion of metal cations and high temperatures or long durations to promote the diffusion. Reaction between solid powder and ammonia gas sometimes results in limited nitridation only at particle surface. To improve the diffusion and homogeneous reaction with ammonia, we applied a new preparation route so called soft chemistry route, in which an amorphous oxide precursor obtained through firing of citrate or glycine gel was nitrided under an ammonia flowing. Homogeneous mixing of metal cations was achieved in water or ethanol solution as shown in **Fig. 1**(a). After mixing of appropriate amount of citric acid or glycine as a peptizer, the solution was heated at around 120°C to obtain a viscous gel. The gel was then fired to be an amorphous oxide precursor [Fig. 1(b)]. High homogeneity and amorphous nature of the precursor can enhance the reactivity with ammonia gas resulting in formation of novel oxynitride compounds in high purity.

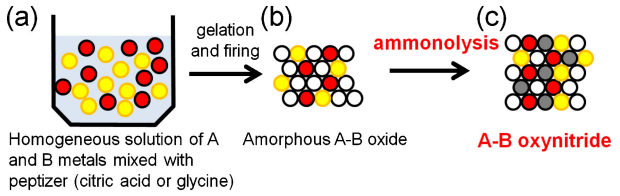

Fig. 1. (Color online) Schematic diagram of ammonolysis reaction process through citrate route. (a) starting powders were dissolved in water or ethanol solution with a peptizer, (b) the solution turned to gel and then firing to get amorphous oxide precursor, and (c) the precursor was nitrided under an ammonia flowing to form an oxynitride.

In this review, preparation of novel oxynitride materials by ammonolysis of amorphous precursors obtained through citrate or glycine gel are reported. Their crystal structure analyzed by using neutron diffraction or transmission electron microscopy was investigated in relation to their properties. Crystal structure of perovskite type dielectric oxynitride $SrTaO_2N$ was refined by using neutron diffraction to elucidate its anionic distribution and displacement to understand the dielectric behavior (section 2.1.).

† Corresponding author: Y. Masubuchi; E-mail: yuji-mas@eng.hokudai.ac.jp

Its dense ceramics were obtained by pressureless sintering with sintering additive showing superior dielectric properties (section 2.2.). In section 3, stacking disorder of gallium oxynitride observed by using scanning transmission electron microscopy and optical property of as-grown gallium oxynitride nanowires are shown. We have also prepared novel oxynitride phosphor material doped with europium having a magnetoplumbite structure and investigated its emission site splitting in section 4.

2. Dielectric perovskite oxynitride $SrTaO_2N$

2.1 Local anionic ordering in $SrTaO_2N$

Recently, Kim, et al., reported that $BaTaO_2N$ and $SrTaO_2N$ possessed a large permittivity of ca. 4900 and 2900 with moderate temperature dependence.[12] They are oxynitride derivatives of $BaTiO_3$ and $SrTiO_3$. To date, crystal structure of $BaTaO_2N$ has been mainly discussed with the unusual dielectric behavior.[23)–25)] Although the crystal structure of $BaTaO_2N$ was refined in space group of *Pm*-3*m*,[26] local structure around Ta octahedral was suggested to induce its dielectric polarization. Direct observation of the anionic ordering or distortion is impossible by using diffraction method, because there is only one anionic site in the cubic structure model. In contrast to $BaTaO_2N$, the number of studies on crystal structure and dielectric property has been limited in perovskite-type $SrTaO_2N$. Its crystal structure has been refined in tetragonal *I*4/*mcm* models with discrepant anionic occupations.[12),22),27)] Both a complete O/N ordering[27] and a statistical anion distribution among the available sites[22] were reported. It was possible to analyze a local anionic deviation in the space group of *I*4/*mcm* because there are two crystallographic sites in $SrTaO_2N$. Therefore, crystal structure of $SrTaO_2N$ focusing on anionic site occupancy and local displacement were investigated to elucidate the origin of the unusual dielectric property of $SrTaO_2N$. Neutron diffraction analysis is particularly appropriate to study local anionic structure and preferential occupation in the oxynitride, because of the considerably different neutron scattering lengths for O (5.803 fm) and N (9.360 fm).[28]

The peroskite-type $SrTaO_2N$ was prepared by ammonolysis of precursor obtained through citrate gel. A stoichiometric amount of $SrCO_3$ and $TaCl_5$ was dissolved in ethanol with an equimolar of citric acid as a peptizer. The solution was heated under stirring on hot plate to obtain a viscous gel. The gel was then pre-fired in a box furnace, resulting in brownish amorphous oxide precursor. The precursor was nitrided under an ammonia flow of 50 mL/min at 1000°C for 12 h. Phase purity was checked by using X-ray diffraction. Neutron diffraction measurements were performed at room temperature using the high resolution powder diffractometer (HERMES) installed at the JRR-3M reactor of the JAEA.[29] The Rietveld program RIETAN-2000 was used for structural refinements.[30] The refined crystal structure was visualized using VESTA program.[31]

Single phase of perovskite-type $SrTaO_2N$ was obtained by the ammonolysis reaction. Its structure refinement was performed based on the tetragonal *I*4/*mcm* model.[32] **Figure 2**(a) indicates the refined crystal structure of $SrTaO_2N$. The site occupations of nitride ions is always higher at the axial 4*a* site than the equatorial 8*h* site with the occupancies of O/N ≈ 0.5/0.5 and 0.75/0.25 for the former and the latter, respectively. This result is in good agreement with that reported by Clark et al.[22] It should be noted that such preferential site occupations are little dependent on the synthesis route, because the crystal structure of $SrTaO_2N$ obtained by nitridation of oxide precursors was well refined in similar anionic occupancies. The site preference feature of $SrTaO_2N$, in which both half of the axial 4*a* site and quarter of

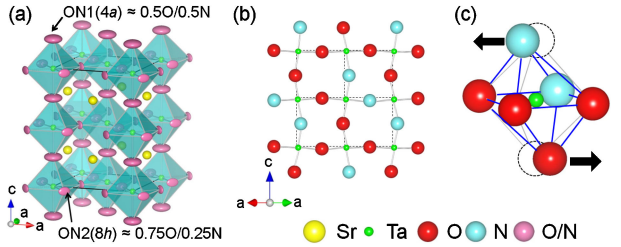

Fig. 2. (Color online) (a) refined crystal structure image of perovskite $SrTaO_2N$. In this image, the anisotropic displacements are shown as ellipsoids. (b) schematic local tilting of tantalum octahedral with anionic displacement. (c) local *cis* configuration in TaO_4N_2 octahedron.

the equatorial 8*h* site are occupied by nitride ions, indicate each TaO_4N_2 octahedron displays a *cis* configuration with one nitride ion at the axial site and the other at the equatorial site as shown in Fig. 2(c). Such local symmetry reduction in $SrTaO_2N$ was already suggested by theoretical calculations[33] and EXAFS measurement,[16] because of a shorter Ta–N bond length than Ta–O. Local symmetry lowering was also suggested from electron diffraction analysis on $SrTaO_2N$ showing weak extra reflections that should be absent in the *I*4/*mcm* model.[34] The local O/N ordering was suggested to occur up to 750°C.[34] Large anisotropic displacement parameter in *ab* plane was also observed at the axial 4*a* site, as shown in Fig. 2(a). The extraordinary large displacement in *ab* plane implies that anions at the axial 4*a* site deviate within *ab* plane in a statistical way. Together with the smaller displacement for the 8*h* site, these anionic displacements suggest that the TaO_4N_2 octahedra are likely to tilt each other along *c*-axis, as shown in Fig. 2(b). Figure 2(b) indicates TaO_4N_2 network including local O/N ordering with *cis* configuration and anisotropic displacements. Short-range O/N ordering and octahedral tilting, giving rise to the local distortion, are schematically displayed in this image. Because of the differences in the interatomic distance and covalency of Ta–O and Ta–N bonds, local O/N ordering involving *cis* configuration of nitride ions might induce tilting of each TaO_4N_2 octahedron and thereby the development of local polarization. The unusually larger permittivity of $SrTaO_2N$ could be closely related to the octahedral tilting. It should be noted that such local distortion is not correlated over a large length scale and therefore a statistically-averaged centrosymmetric crystal structure (space group *I*4/*mcm*) is achieved. The nonzero polar momentum local units in $SrTaO_2N$ make it exhibit excellent dielectric behavior under applied field.

2.2 Sintering and dielectric properties of $SrTaO_2N$ ceramics

The origin of large dielectric permittivity of $SrTaO_2N$ was investigated in relation to its local anion ordering with octahedral tilting, resulting in the nonzero polar momentum units under applied field. One of the problems pertaining to dielectric oxynitride ceramics is the difficulty in fabricating high-density ceramics. There are only a few reports on dielectric oxynitrides,[12)–16)] especially in the ceramic form.[12] The reported bulk density of $SrTaO_2N$ was very low about 45% when it was sintered by using a conventional method. Therefore, the densification of $SrTaO_2N$ ceramic is necessary for fundamental characterization and also for practical applications. Pressureless sintering method with certain additives was applied for a densification of the oxynitride. The sintering of dielectric perovskite oxide can be promoted by the addition of A-site donor dopants because the densification kinetics is enhanced by the subsequently induced

A-site defects.[35)–37)] During the sintering process, incorporation of suitable additives could compensate the loss of easy-to-volatilize components, such as PbO in PMN and SrO in $SrTiO_3$.[38),39)]

$SrTaO_2N$ oxynitride powder was obtained by above mentioned method. The obtained oxynitride powders were mixed with 5 wt % of $SrCO_3$ as an sintering additive. These powders were die-pressed into 7 mm diameter and 2 mm thick disks, followed by cold isostatic pressing at 150 MPa. The disks were placed in a BN crucible and sintered at 1400°C for 3 h under a nitrogen pressure of 0.2 MPa using a graphite furnace. The sintered bulks were then annealed at 1000°C for 12 h under an ammonia flowing. This post-annealing process was necessary to obtain highly resistive bulks for reliable dielectric property measurement.

As-sintered $SrTaO_2N$ without $SrCO_3$ additive was contaminated with a small amount of TaC. The TaC impurity is likely to be formed when excess Ta is combined with organic residue due to the loss of SrO from $SrTaO_2N$ during sintering. In spite of high melting temperature, loss of SrO may occur in high temperature processing, as reported in $SrTiO_3$, $SrZrO_3$ and Sr_2RuO_4.[39)–41)] The impurity phase disappeared in the as-sintered $SrTaO_2N$ bulk with $SrCO_3$ additive because of Sr^{2+} from the additive compensates the Sr loss,[42)] which inhibits the appearance of the secondary phase. However, sintered bulks both with and without sintering additive changed their color from brown to dark grey, indicating reduction of the tantalum associated with anion deficiencies in the crystal lattice. Post-annealing in an ammonia atmosphere was necessary to recover their original color to brown and oxidation state of tantalum cation. After the annealing process, TaC and Ta_3N_5 impurities were observed in $SrTaO_2N$ bulk without additive, while the annealed bulk with additive was perovskite single phase.

The relative densities of the post-annealed $SrTaO_2N$ bulks without and with sintering additive were 70% and 93%, respectively. The $SrTaO_2N$ bulk without additive could not be sintered well, while a high density was achieved at 1400°C by the addition of 5 wt % of $SrCO_3$. The fracture surface morphology was changed by the addition of sintering additive as shown in **Fig. 3**. After the annealing process, densification and smaller grain size were achieved with the sintering additives. The SrO from $SrCO_3$ additive might react with Sr-deficient $SrTaO_2N$ to promote the efficient reaction sintering and further densification, while no obviously segregated compounds such as strontium tantalum oxide was observed in the microstructure. All the as-sintered $SrTaO_2N$ bulk exhibited a semiconductive behavior, typically with several thousand ohms at room temperature. The successive annealing under the ammonia flowing was found to be essential to recover the dielectric properties which accompanied resistance values several order of magnitudes larger than those of the as-sintered bulks. Dielectric constant (ε_r) and dielectric loss ($\tan\delta$) as a function of frequency for the post-annealed $SrTaO_2N$ bulks are shown in **Fig. 4**. Both dielectric constant and dielectric loss gradually decrease with increasing frequency. The $SrTaO_2N$ bulk without additive have ε_r in the order of 1.8×10^3 at 10^2 Hz. In contrast, the addition of $SrCO_3$ resulted in a significant increase in the dielectric constant, which is about 3.6×10^4 at 10^2 Hz. This value is several times higher than the permittivity (~2900) reported by Kim et al.[12)] The permittivity of $SrTaO_2N$ bulk with additive is comparable to those reported for ferroelectric and relaxor oxides at their Curie temperatures.[43)] Frequency dependence of dielectric constant is very small. The dielectric constants of the $SrTaO_2N$ ceramic are sensitive to its density. Enhanced densification is beneficial to obtain desirable dielectric properties. The annealed $SrTaO_2N$ with additive has

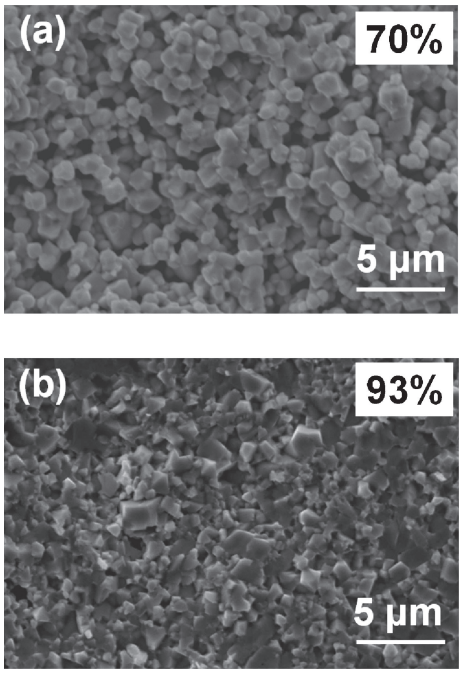

Fig. 3. Scanning electron micrographs of the fracture surface of post-annealed (a) $SrTaO_2N$ without additive, and (b) $SrTaO_2N$ with $SrCO_3$ additive.[42)]

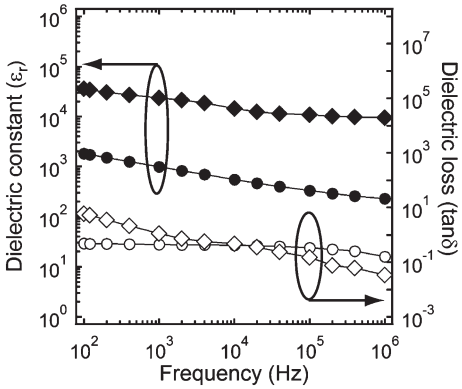

Fig. 4. Relative dielectric constants (ε_r) and dielectric loss ($\tan\delta$) of post-annealed $SrTaO_2N$ without additive (circles) and with additive (diamonds).

a significantly improved grain microstructure, but the dielectric loss is relatively high. The $\tan\delta$ values are approximately 0.04 at 1 MHz, which is still higher than that required for practical applications. The formation of lattice defects within the crystal lattice can affects the dielectric loss. The $SrTaO_2N$ bulk with additive are well densified, therefore it is likely that the anion deficiencies were not completely removed during the post annealing process. A small amount of anion vacancies or tetravalent tantalum cation is sufficient to cause a large increase in the dielectric loss. It should be further reduced by eliminating anion vacancies in a considerably improved microstructure.

3. Gallium oxynitride nanowire

3.1 Direct observation of biphasic wurtzite and zinc-blende structure

Gallium nitride (GaN) and the related materials have been widely studied for various applications including UV-blue light emitting diodes, laser diodes and UV detectors.[44)–46)] Their nano-

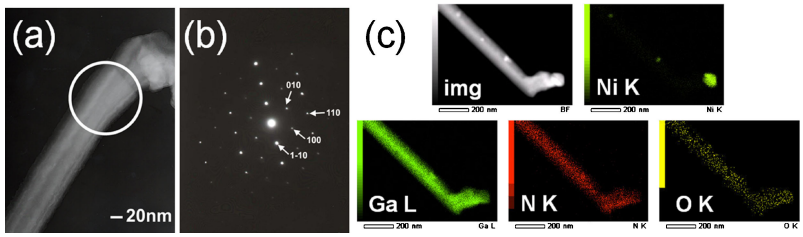

Fig. 5. (Color online) Typical TEM image of GaON nanowire (a) and its electron diffraction obtained by perpendicular electron irradiation (b). Scanning TEM and elemental mapping images of GaON nanowire (c).

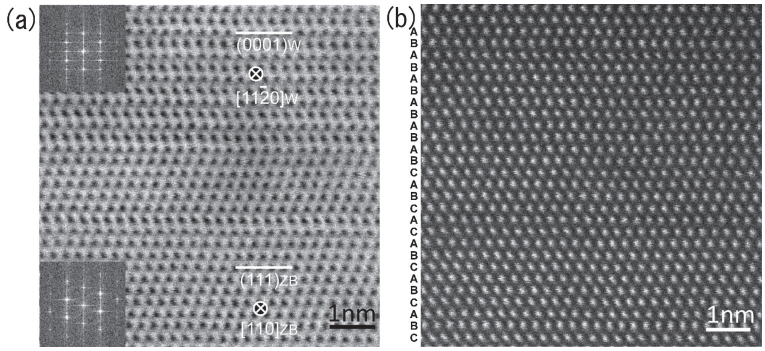

Fig. 6. (a) BF-STEM image of GaON nanowire. Incident electron beam along [11–20] and [110] zone axes in hexagonal wurtzite and its corresponding cubic zinc-blende lattice. (b) HAADF-STEM image of GaON nanowire. A, B and C indicate the stacking sequence.[65]

wires have been attracting interest for a wide range of optical and electronic applications, such as a UV lasers, field effect transistors and logical gates.[47)–49)] Nanowires can be grown by various methods using metal catalysis for vapor–liquid–solid (VLS) growth mechanism.[49)–53)] Theoretical calculations predicted that spinel type gallium oxynitride γ-Ga_3O_3N will be formed from β-Ga_2O_3 and GaN under high pressure and be stabilized by introduction of gallium vacancies.[54),55)] Spinel type gallium oxynitride including both gallium ions and anion vacancies were obtained by high pressure synthesis.[56)] Gallium oxynitride (GaON) with a wurtzite-like structure was firstly prepared by ammonolysis of $NiGa_2O_4$.[11)] Its crystal structure has been expected to be 6H polytypoid, because of coexisting of characteristic Raman bands for wurtzite (2H) and zinc-blende (3C).[57)] Our group has prepared wurtzite-type GaON with a chemical composition of $(Ga_{0.89}\square_{0.11})(O_{0.33}N_{0.67})$ by ammonolysis of amorphous gallium oxide precursors obtained through the citrate route,[58)] where the symbol $\square$ indicates a gallium site vacancy. Some kinds of 3d transition metals were doped into the GaON to study the magnetic properties by using similar preparation methods.[59)–62)] Ammonolysis of an amorphous gallium oxide precursor containing a few percent of Ni or Co additives produced GaON nanowires mixed with agglomerated GaON grains.[63)] The nanowires grew to length of several micrometers and widths of several tens of nanometers at an ammonolysis temperature of 750°C, as shown in **Fig. 5**(a). Their electron diffraction pattern indicates that they grew parallel to the hexagonal *c*-plane [Fig. 5(b)]. Ni or Co additives were found in the agglomerated grains, but not in the GaON nanowires as depicted in Fig. 5(c). The GaON nanowires were assumed to be grown by the catalytic behavior of Ni or Co, which precipitated during ammonolysis due to the instability of their nitrides.[64)] One-dimensional growth occurred because the metal precipitates obstruct isotropic two-dimensional growth of GaON in the hexagonal *c*-plane. The nanowire did not grow by VLS growth. They should be single crystals with a fixed chemical composition. They were expected to have a highly disordered wurtzite (2H) crystal structure with some zinc-blende (3C) type stacking disorders based on X-ray diffraction patterns of the mixture of nanowires and agglomerated grains.

Structural characteristics of the GaON nanowire were first observed directly by using scanning transmission electron microscopy (STEM). **Figure 6**(a) shows a bright-field (BF) STEM image of a GaON nanowire.[65)] In this image the lateral direction is the nanowire growth direction. The BF-STEM image and its corresponding Fourier transforms indicate that the GaON nanowire consists of wurtzite and zinc-blende lattices. The close-packed planes i.e. the *c*-plane in wurtzite and the (111) plane in zinc-blende, are parallel to the nanowire growth direction. Figure 6(b) shows a high-angle annular dark field (HAADF) STEM image taken from the same area shown in Fig. 6(a). In HAADF-STEM images, signal intensity is known to be roughly proportional to the square of the atomic number Z.[66)] The bright spots in the image correspond to gallium ions. ABAB and ABCABC stacking sequences of gallium ions correspond to wurtzite and zinc-blende lattices, respectively. They are clearly observed in the upper and lower regions of the image. A stacking disorder of about six atomic layers is sandwiched between them. GaON nanowires were assumed to grow by catalytic behavior of Ni or Co which obstructs isotropic two-dimensional crystal growth in the hexagonal *c*-plane.[63)] The mononitride of nickel and cobalt has been reported to crystallize in the zinc-blende structure.[64)] The presence of Ni or Co during ammonolysis of amorphous gallium oxide may induce the observed biphasic stacking of GaON nanowires because nickel and cobalt nitride crystallize in the zinc-blende structure, whereas GaON prepared by ammonolysis of amorphous gallium oxide precursor has the wurtzite structure.[58)] The present STEM-EDX observations showed that the GaON nanowires prepared at 750°C contained about 30 at. % of oxide ions substituted for nitride ions. In order to keep its charge neutrality, some gallium site must be vacant.

Gallium vacancies and incorporated oxide ions may introduce stacking disorder into the GaON lattice. α-Ga_2O_3 crystallizes in the corundum structure in which one third of the octahedral sites are vacant in hcp.[67] GaN has the wurtzite structure in hcp and β-Ga_2O_3 crystallizes in the ccp with partially occupied tetrahedral and octahedral sites.[68),69)] The different stacking in simple gallium compounds may suggest understanding of the complicated stacking in relation to the gallium vacancy.

3.2 Crystal growth and characterization of gallium oxynitride nanowire

GaON nanowires were grown from seed crystals separated from an agglomerated grains prepared by ammonolysis of amorphous gallium oxide precursor with Ni additives, in order to perform its optical and electrical measurements.[70)] As nitrided GaON nanowire mixed with agglomerated grains were ultrasonically dispersed in acetone. The suspended solution was then dropped onto a silica glass substrate to use the GaON nanowires as seed crystals for subsequent nanowire growth. The seed crystals on the substrate were placed in a tube furnace with the gallium oxide precursor, which had been prepared through citrate route without Ni or Co additives. The seed crystals and the precursor were annealed under an ammonia flowing.

The morphologies of the products obtained by annealing under ammonia flowing varied depending on the growth temperature.[70)] The nanowires grew to a maximum length of 150 µm from seed crystals of several micrometers long, but did not grow laterally at 750 and 800°C as shown in **Figs. 7**(a) and 7(b). A large amount of ca. 10 µm long GaON nanowires was observed together with long nanowires at 900°C [Fig. 7(c)]. The former were intertwined with each other and had similar widths as those of the seed crystals. The morphology changed drastically at 1000°C [Fig. 7(d)]. Needle like crystals that were several micrometers wide and several tens of micrometers long grew together with thin nanowires with similar widths as the seed crystals. A different nucleation mechanism may be responsible for the growth of the large amount of nanowires at 900°C and needle like crystal at 1000°C independent from the seed crystals. Significant amount of gallium-containing vapors such as Ga_2O were reported to be generated from β-Ga_2O_3 above 900°C.[71)] Excess supply of gallium vapor might increase GaON nucleation on the surface of seed crystals. The nanowires grown at 750 and 800°C showed hexagonal patterns in their TEM-ED when the electron beam is irradiated perpendicular to the nanowire, indicating the nanowires grew parallel to the hexagonal *c*-plane along the seed crystals. GaON nanowires grown at 900 and 1000°C contained nanowires that grew along the seed crystal, (i.e. parallel to the hexagonal *c*-plane), although some nanowires grew in different directions. Similar growth has been reported for GaN nanowires, which were grown by the VLS mechanism.[72),73)] At 900 and 1000°C, as-grown nanowires may contaminate with GaN-like nanowires resulting in growth in different directions from the seed crystal.

Cathodoluminescence (CL) spectra were obtained from GaON nanowires grown at 800 and 1000°C as shown in **Fig. 8**. The GaON nanowire grown at 1000°C exhibited strong emission at about 3.4 eV and weak blue emission at 2.9 eV. The former has been assigned to band gap emission of GaN.[74)] Blue emission from wurtzite GaN has been reported to be related to complex defects due to gallium vacancies formed by the substitution of nitride ions with oxide ions.[75)] The blue emission at 2.9 eV implied the GaON nanowires grown at 1000°C contain gallium vacancies coexisting with oxide ions substituting nitride ions in GaN-like crystal. The blue emission was also observed in the

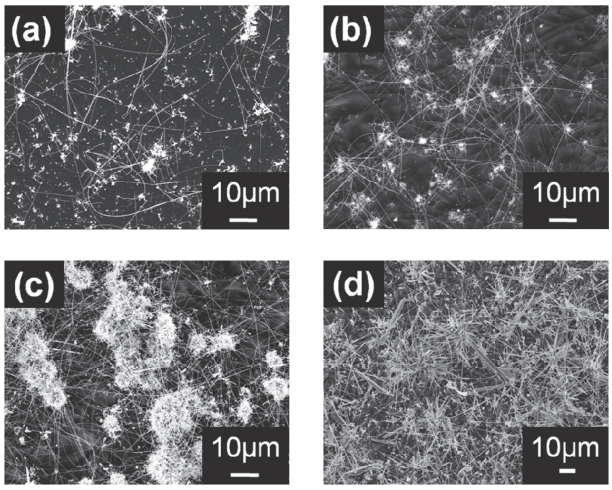

Fig. 7. SEM images of GaON nanowires grown at (a) 750, (b) 800, (c) 900, and (d) 1000°C.[70)]

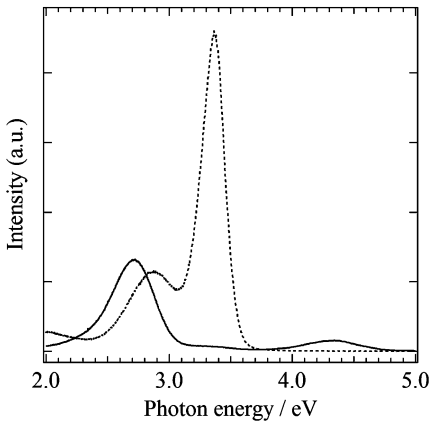

Fig. 8. Room temperature CL spectra of GaON nanowires grown at 800 (solid line) and 1000°C (dashed line).

GaON nanowire grown at 800°C, with small but apparent UV emission at 4.3 eV. Large band gap energy of 4.8 eV has been reported in single crystals of β-Ga_2O_3.[76)] The observed UV emission at 4.3 eV implied the band structure of GaON nanowires grown at 800°C were similar to that of gallium oxide not to gallium nitride, maybe due to introduction of large amount of oxide ions in the GaON nanowire. STEM-EDX revealed that about 30 at. % of nitride ions was substituted by oxide ions in GaON nanowires grown below 800°C. The blue emission at 2.7 eV of the nanowire grown at 800°C might also originate in complex defect levels formed by gallium vacancies and nitride/oxide ions in gallium oxide like band structure, not in gallium nitride, as suggested for blue emissions of β-Ga_2O_3.[77)]

The electrical conductivity was estimated by dc four-probe method with Pt electrodes formed by electron-beam lithography. Nanowires grown at 900°C had an n-type electrical conductivity of 76–116 $S \cdot cm^{-1}$ with an activation energy of about 1 meV in the temperature range 130 to 330 K. This is similar to the values obtained for nanowires grown at 750°C. The GaON nanowires were excited by 393 nm light (3.15 eV), which is a lower energy than the band gap observed in the CL spectra. For both nanowires, the photocurrent increased under UV light irradiation and it had a long decay time when the irradiation was turned off. Such persistent photoconductivity (PPC) has been observed on n-type GaN; it was assigned to unintended Ga vacancies without ele-

mental doping.[78),79)] The present GaON nanowires have gallium vacancies that were intentionally induced by introducing oxide ions to the GaON lattice. The observation of PPC in the nanowires suggests that the GaON nanowires grown in this study contain gallium vacancies formed by oxide ions introduced into the GaN lattice even at the high-temperature crystal growth.

4. Emission site splitting in magnetoplumbite type aluminum oxynitride phosphor

White light emitting diodes (LEDs) have received much attention as high efficiency, safe and environmentally friendly devices.[5)] For white LED applications, SiAlON related phosphor materials have been developed to improve color rendering properties.[5),6),17),19)] In white LEDs with multiple phosphor components, the color balance must be controlled. Recently, single component phosphors that exhibit multiple color emission have emerged to improve the color balance.[80),81)] Our group reported three emission peaks for Eu^{2+} doped AlON with an impurity phase of magnetoplumbite (MP)-type $EuAl_{12}O_{19}$.[82)] The multiple emissions were attributed to the presence of the different coordination environments around Eu^{2+} with different O/N rations in the MP structure. However, crystal structure and photoluminescense property of MP-type oxynitride has not yet been reported.

MP-type Eu doped lanthanum aluminum oxynitride [$LaAl_{12}(O,N)_{19}$] was prepared using aluminum glycine gel precursors followed by post annealing of the nitrided precursors.[83)] Aluminum acetylacetonate, lanthanum acetylacetonate hydrate and europium acetylacetonate hydrate were used as starting materials. Those powders were mixed in anhydrous ethanol with glycine as a peptizer. The solution was heated on a hot plate to obtain gelatinous products. The gel was pre-fired in air at 500°C for 1 h and then nitrided at 850°C under an ammonia flowing. The nitrided products were post-annealed at 1700°C in a gas pressure furnace for 3 h under a nitrogen gas pressure of 0.2 MPa to improve their crystallinity.

5 at. % Eu doped $LaAl_{12}(O,N)_{19}$ exhibited broad blue emission at 440 nm with a shoulder peak at 464 nm under excitation at 254 nm as shown in **Fig. 9**. No characteristic sharp peaks due to Eu^{3+} ions were observed, which confirms the presence of only Eu^{2+} ions in the oxynitride phosphor. The product exhibited broad excitation spectrum between 250 and 360 nm for the emission at 440 nm. Single phase of 5 at. % Eu doped $CaAl_{12}O_{19}$ was obtained in a conventional solid state reaction, which showed a single broad emission at 415 nm. The emission wavelength was shorter than that for Eu-doped $LaAl_{12}(O,N)_{19}$. It is believed that the long wavelength emission is attributed to covalent bond character and a large crystal field splitting effect on Eu^{2+} 5*d* band.[84)] The present red-shift of the emission peak wavelength may be caused by the introduction of nitride ions to increase the covalent character.

The crystal structure of 3 at. % Eu-doped $LaAl_{12}(O,N)_{19}$ was refined in the MP structural model using its neutron diffraction data.[83)] Anomalously large isotropic displacement parameter on the lanthanum site was observed when single lanthanum site (2*d*) was applied. The large displacement parameter implied lanthanum site splitting. The refinement was improved by dividing the lanthanum site from the original 2*d* site to 2*d* and 6*h* sites. The isotropic displacement on the lanthanum sites was refined to a reasonable value. Doped europium ion was refined to occupy both lanthanum sites. Crystal structure of $CaAl_{12}O_{19}$ doped with Eu was also refined in MP structure without calcium site splitting. The atomic arrangements around the lanthanum and calcium sites in the MP-type oxynitride and oxide are shown in **Fig. 10**. The original 2*d* sites (RE1 and CA1) are in similar coordination

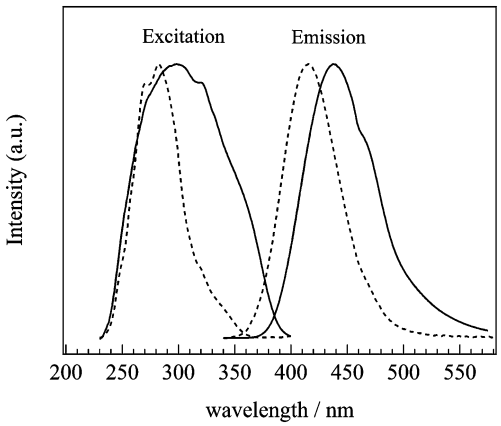

Fig. 9. Emission and excitation spectra for MP-type $La_{0.95}Eu_{0.05}Al_{12}(O,N)_{19}$ (solid line) and $Ca_{0.95}Eu_{0.05}Al_{12}O_{19}$ (broken line). Emission spectra were measured under excitation at 254 nm and excitation spectra were monitored at 440 and 415 nm for $La_{0.95}Eu_{0.05}Al_{12}(O,N)_{19}$ and $Ca_{0.95}Eu_{0.05}Al_{12}O_{19}$, respectively.[83)]

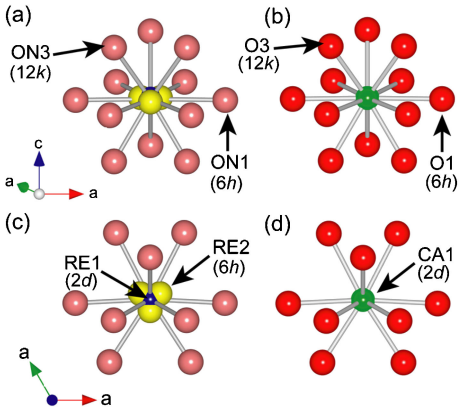

Fig. 10. (Color online) Atomic arrangements around the lanthanum and calcium site in MP-type (a, c) $LaAl_{12}(O, N)_{19}$:Eu and (b,d) $CaAl_{12}O_{19}$:Eu. These structures were visualized with the VESTA program,[31)] using the refined structural parameters. The structure in (c) and (d) are viewed along the *c*-axis.[83)]

environments to each other in the respective crystal structure. The bond length of La–N is approximately 0.265 nm in LaN and longer than that of La–O (0.258 nm) in La_2O_3.[85),86)] Some of La ions are shifted in their position from the 2*d* site to the 6*h* site so as to be apart from the introduced nitride ion, resulting in lanthanum site splitting in the oxynitride structure. The emission peak splitting observed in the oxynitride can be attributed to Eu site splitting into the 2*d* and 6*h* sites. The 6*h* site has lower symmetry than the 2*d* site and its coordination number may be decreased from 12 (2*d*) to 10 (6*h*), as shown in Fig. 10. Lower symmetry and smaller coordination number results in an increase in the crystal field splitting effect on Eu^{2+}, which results in the red-shift emission. The emission peak at 440 nm and the shoulder at 460 nm can be caused by emission from Eu^{2+} on the 2*d* and 6*h* sites, respectively.

5. Conclusions

Novel metal oxynitrides have been prepared by ammonolysis of amorphous metal oxide obtained from citrate or glycine gel. Their crystal structure, especially in O/N distribution and local bonding characteristics has been analyzed to investigate their electric and optical properties. In the dielectric $SrTaO_2N$ perovskite, the

short range O/N ordering as *cis* configuration of nitride ions and local tilting of TaO_4N_2 octahedra were suggested from neutron diffraction analysis, contributing to the unusual dielectric behavior. Its sintered bulks having a relative density above 90% were prepared by pressureless sintering using $SrCO_3$ additive. The $SrTaO_2N$ dense ceramics exhibited superior dielectric constant above 1×10^4 and dielectric loss of 0.04 at a frequency of 1 MHz. New biphasic wurtzite and zinc-blende structure of GaON nanowire was first observed by using STEM. The biphasic structure formed due to the presence of Ni or Co in starting material because their nitride has a zinc-blende structure whereas gallium oxynitride has the wurtzite structure. GaON nanowire grown at 800°C exhibited characteristic broad UV emission at 4.3 eV in its cathodoluminescence spectrum, while GaN like emission at around 3.4 eV was not observed. These facts implied the band structure of GaON is similar to that of gallium oxide (band gap of 4.8 eV) rather than that of GaN due to introduction of large amount of oxide ions in GaON nanowires. Eu doped lanthanum aluminum oxynitride with magnetoplumbite structure exhibited emission peak splitting. Neutron diffraction study of the oxynitride indicated that the lanthanum site partially occupied by Eu^{2+} splits into 2*d* and 6*h* sites. The emission peak splitting of the oxynitride is not directly related to two kinds of anions, but to the Eu^{2+} site splitting induced by the two kinds of anions.

Many kinds of oxynitride ceramics have been prepared in the last decades, because of much interest for new applications and scientific investigations. In oxynitride materials, not only chemical composition, i.e. O/N ratio, but also local O/N distribution has been important to elucidate their characteristic properties. Studies on practical applications, such as densification, thin film fabrication, and mass production, will be strongly expected for the future as well as development of new oxynitride materials.

Acknowledgements The author thanks Professors Shinichi Kikkawa and Teruki Motohashi of Hokkaido University for their kind support during the present works and for their helpful suggestions and comments. The author also acknowledges Professors Yuichi Ikuhara, Teruyasu Mizoguchi, and Tetsuya Tohei of The University of Tokyo for their TEM observations, Professor Takashi Sekiguchi, Dr. Kentaro Watanabe, and Dr. Woong Lee of NIMS for their CL measurements and Dr. Kazuhiro Kirihara of AIST for his electrical property measurements. A part of this study was funded by Grant-in-Aid for Scientific Research from Ministry of Education, Culture, Sports, Science and Technology (MEXT) of Japan and from the Japan Society for the Promotion of Science (JSPS). Author also acknowledges financial support from the Global COE Program (Project no. B01: "Catalysis as the basis for innovation in materials science") from MEXT of Japan. Neutron diffraction measurements were performed under the approvals in the JRR-3M reactor as JAEA.

References

1) R. Marchand, Y. Laurent, J. Guyader, P. L'Haridon and P. Verdier, *J. Eur. Ceram. Soc.*, **8**, 197–213 (1991).
2) R. Marchand, "Handbook on the Physics and Chemistry of Rare Earths", vol. 25, Ed. by K. A. Gschneider Jr. and L. Eyring, Elsevier, Amsterdam (1998) pp. 51–99.
3) R. Marchand, F. Tessier, A. L. Sauze and N. Diot, *Int. J. Inorg. Mater.*, **3**, 1143–1146 (2001).
4) F. Tessier and R. Marchand, *J. Solid State Chem.*, **171**, 143–151 (2003).
5) R. J. Xie, N. Hirosaki, K. Sakuma, Y. Yamamoto and M. Mitomo, *Appl. Phys. Lett.*, **84**, 5404–5406 (2004).
6) T. Suehiro, N. Hirosaki, R. J. Xie and M. Mitomo, *Chem. Mater.*, **17**, 308–314 (2005).
7) K. Maeda and K. Domen, *J. Phys. Chem. C*, **111**, 7851–7861 (2007).
8) K. Maeda, T. Takata, M. Hara, N. Saito, Y. Inoue, H. Kobayashi and K. Domen, *J. Am. Chem. Soc.*, **127**, 8286–8287 (2005).
9) M. Jansen and H. P. Letschert, *Nature*, **404**, 980–982 (2000).
10) M. Pérez-Estébanez, R. Pastrana-Fábregas, J. Isasi-Marín and R. Sáez-Puche, *J. Mater. Res.*, **21**, 1427–1433 (2006).
11) M. Kerlau, O. Merdrignac-Conanec, P. Reichel, N. Bâsan and U. Weimer, *Sens. Actuators, B*, **115**, 4–11 (2006).
12) Y. I. Kim, P. M. Woodward, K. Z. Baba-Kishi and C. W. Tai, *Chem. Mater.*, **16**, 1267–1276 (2004).
13) Y. I. Kim, W. Si, P. M. Woodward, E. Sutter, S. Park and T. Vogt, *Chem. Mater.*, **19**, 618–623 (2007).
14) A. Ziani, C. Le Paven-Thivet, L. Le Gendre, D. Fasquelle, J.-C. Carru, F. Tessier and J. Pinel, *Thin Solid Films*, **517**, 544–549 (2008).
15) Y. Lu, A. Ziani, C. Le Paven-Thivet, R. Benzerga, L. Le Gendre, D. Fasquelle, H. Kassem, F. Tessier, V. Vigneras, J.-C. Carru and A. Sharaiha, *Thin Solid Films*, **520**, 778–783 (2011).
16) S. G. Ebbinghaus, H. P. Abicht, R. Dronskowski, T. Müller, A. Reller and A. Weidenkaff, *Prog. Solid State Chem.*, **37**, 173–205 (2009).
17) N. Hirosaki, R. J. Xie, K. Kimoto, T. Sekiguchi, Y. Yamamoto, T. Suehiro and M. Mitomo, *Appl. Phys. Lett.*, **86**, 211905 (2005).
18) R. J. Xie, N. Hirosaki, X. J. Liu, T. Takeda and H. L. Li, *Appl. Phys. Lett.*, **92**, 201905 (2008).
19) K. Uheda, N. Hirosaki and H. Yamamoto, *Phys. Status Solidi (a)*, **203**, 2712–2717 (2006).
20) R. Assabaa-Boultif, R. Marchand, Y. Laurent and J. J. Videau, *Mater. Res. Bull.*, **29**, 667–672 (1994).
21) S. J. Clarke, B. P. Guinot, C. W. Michie, M. J. C. Calmont and M. J. Rosseinsky, *Chem. Mater.*, **14**, 288–294 (2002).
22) S. J. Clarke, K. A. Hardstone, C. W. Michie and M. J. Rosseinsky, *Chem. Mater.*, **14**, 2664–2669 (2002).
23) C. M. Fang, G. A. de Wijs, E. Orhan, G. de With, R. A. de Groot, H. T. Hintzen and R. Marchand, *J. Phys. Chem. Solids*, **64**, 281–286 (2003).
24) B. Ravel, Y. I. Kim, P. M. Woodward and C. M. Fang, *Phys. Rev. B*, **73**, 184121 (2006).
25) K. Page, M. W. Stoltzfus, Y.-I. Kim, Th. Proffen, P. M. Woodward, A. K. Cheetham and R. Seshadri, *Chem. Mater.*, **19**, 4037–4042 (2007).
26) F. Pors, R. Marchand, Y. Laurent, P. Bacher and G. Roult, *Mater. Res. Bull.*, **23**, 1447–1450 (1988).
27) E. Günther, R. Hagenmayer and M. Jansen, *Z. Anorg. Allg. Chem.*, **626**, 1519–1525 (2000).
28) T. Proffen, V. Petkov, S. J. L. Billinge and T. Vogt, *Z. Kristallogr.*, **217**, 47–50 (2002).
29) K. Ohoyama, T. Kanouchi, K. Nemoto, M. Ohashi, T. Kajitani and Y. Yamaguchi, *Jpn. J. Appl. Phys.*, **37**, 3319–3326 (1998).
30) F. Izumi and T. Ikeda, *Mater. Sci. Forum*, **321–324**, 198–203 (2000).
31) K. Momma and F. Izumi, *J. Appl. Cryst.*, **41**, 653–658 (2008).
32) Y. R. Zhang, T. Motohashi, Y. Masubuchi and S. Kikkawa, *J. Ceram. Soc. Japan*, **119**, 581–586 (2011).
33) H. Wolff and R. Dronskowski, *J. Comput. Chem.*, **29**, 2260–2267 (2008).
34) M. H. Yang, J. Oró-Solé, J. A. Rodgers, A. B. Jorge, A. Fuertes and J. P. Attfield, *Nat. Chem.*, **3**, 47–52 (2011).
35) A. Banerjee, A. Bandyopadhyay and S. Bose, *J. Am. Ceram. Soc.*, **89**, 1594–1600 (2006).
36) B. Malic, J. Bernard, J. Holc, D. Jenko and M. Kosec, *J. Eur. Ceram. Soc.*, **25**, 2707–2711 (2005).
37) P. Fu, Z. Xu, R. Chu, W. Li, G. Zang and J. Hao, *Mater. Des.*, **31**, 796–801 (2010).
38) Y. Yang, C. Feng and Y. Yu, *Mater. Lett.*, **49**, 345–351 (2001).

39) J. G. Bednorz and H. J. Scheel, *J. Cryst. Growth*, **41**, 5–12 (1977).
40) Y. Zhang, D. E. Mack, M. O. Jarligo, X. Cao, R. Vaßen and D. Stöver, *J. Therm. Spray Technol.*, **18**, 694–701 (2009).
41) Y. Pennec, N. J. C. Ingle, I. S. Elfimov, E. Varene, Y. Maeno, A. Damascelli and J. V. Barth, *Phys. Rev. Lett.*, **10**, 216103 (2008).
42) Y. R. Zhang, T. Motohashi, Y. Masubuchi and S. Kikkawa, *J. Eur. Ceram. Soc.*, **32**, 1269–1274 (2012).
43) V. Koval, C. Alemany, J. Briančin, H. Bruncková and K. Saksl, *J. Eur. Ceram. Soc.*, **23**, 1157–1166 (2003).
44) S. Nakamura, T. Mukai and M. Senoh, *Appl. Phys. Lett.*, **64**, 1687–1689 (1994).
45) S. Nakamura, M. Senoh, S. Nagahama, N. Jwasa, T. Tamada, T. Matsushita, H. Kiyoku and Y. Sugimoto, *Jpn. J. Appl. Phys.*, **35**, L74–L76 (1996).
46) I. Akasaki, H. Amano, M. Kito and K. Hiramatsu, *J. Lumin.*, **48–49**, 666–670 (1991).
47) J. C. Johnson, H. J. Choi, K. P. Knutsen, R. D. Schaller, P. Yang and R. J. Saykally, *Nat. Mater.*, **1**, 106–110 (2002).
48) Y. Huang, X. Duan, Y. Cui and C. M. Lieber, *Nano Lett.*, **2**, 101–104 (2002).
49) Y. Huang, X. Duan, Y. Cui, L. J. Lauhon, K. H. Kim and C. M. Lieber, *Science*, **294**, 1313–1317 (2001).
50) S. K. Lee, H. J. Choi, P. Pauzauskie, P. Yang, N. K. Cho, H. D. Park, E. K. Suh, K. Y. Lim and H. J. Lee, *Phys. Status Solidi (b)*, **241**, 2775–2778 (2004).
51) Y. K. Byeun, K. S. Han and S. C. Choi, *J. Electroceram.*, **17**, 903–907 (2006).
52) L. X. Qin, C. S. Xue, H. Z. Zhuang, Z. Z. Yang, H. Li, J. H. Chen and Y. Wang, *Appl. Phys., A Mater. Sci. Process.*, **91**, 675–678 (2008).
53) H. Y. Kwon, M. J. Shin, Y. J. Choi, J. Y. Moon, H. S. Ahn, S. N. Yi, S. Kim, D. H. Ha and S. H. Park, *J. Cryst. Growth*, **311**, 4146–4151 (2009).
54) P. Kroll, R. Dronskowski and M. Martin, *J. Mater. Chem.*, **15**, 3296–3302 (2005).
55) M. Martin, R. Dronskowski, J. Janek, K. D. Becker, D. Roehrens, J. Brendt, M. W. Lumey, L. Nagarajan, I. Valov and A. Borger, *Prog. Solid State Chem.*, **37**, 132–152 (2009).
56) H. Huppertz, S. A. Hering, C. E. Zvoriste, S. Lauterbach, O. Oeckler, R. Riedel and I. Kinski, *Chem. Mater.*, **21**, 2101–2107 (2009).
57) X. Cailleaux, M. C. M. Lucas, O. Merdrignac-Conanec, F. Tessier, K. Nagasaka and S. Kikkawa, *J. Phys. D: Appl. Phys.*, **42**, 045408 (2009).
58) S. Kikkawa, K. Nagasaka, T. Takeda, M. Bailey, T. Sakurai and Y. Miyamoto, *J. Solid State Chem.*, **180**, 1984–1989 (2007).
59) S. Kikkawa, S. Ohtaki, T. Takeda, A. Yoshiasa, T. Sakurai and Y. Miyamoto, *J. Alloys Compd.*, **450**, 152–156 (2008).
60) S. Yamamoto, S. Kikkawa, Y. Masubuchi, T. Takeda, H. Wolff, R. Dronskowski and A. Yoshiasa, *Solid State Commun.*, **147**, 41–45 (2008).
61) S. Yamamoto, S. Kikkawa, Y. Masubuchi, T. Takeda, M. Okube, A. Yoshiasa, M. Lumey and R. Dronskowski, *Mater. Res. Bull.*, **44**, 1656–1659 (2009).
62) A. Miyaake, Y. Masubuchi, T. Takeda and S. Kikkawa, *Mater. Res. Bull.*, **45**, 505–508 (2010).
63) A. Miiyaake, Y. Masubuchi, T. Takeda, T. Motohashi and S. Kikkawa, *Dalton Trans.*, **39**, 6106–6111 (2010).
64) B. Eck, R. Dronskowski, M. Takahashi and S. Kikkawa, *J. Mater. Chem.*, **9**, 1527–1537 (1999).
65) Y. Masubuchi, R. Yamaoka, T. Tohei, T. Mizoguchi, Y. Ikuhara and S. Kikkawa, *J. Eur. Ceram. Soc.*, **23**, 1989–1993 (2012).
66) S. J. Pennycook, B. Rafferty and P. D. Nellist, *Microsc. Microanal.*, **6**, 343–352 (2000).
67) M. Marezio and J. P. Remeika, *J. Chem. Phys.*, **46**, 1862–1865 (1967).
68) G. Kamler, J. Zachara, S. Podsiadlo, L. Adamowicz and W. Gebicki, *J. Cryst. Growth*, **212**, 39–48 (2000).
69) S. Geller, *J. Chem. Phys.*, **33**, 676–684 (1960).
70) Y. Masubuchi, R. Yamaoka, T. Motohashi, K. Kirihara, W. Lee, K. Watanabe, T. Sekiguchi and S. Kikkawa, *J. Cryst. Growth*, **337**, 87–92 (2011).
71) H. Kiyono, T. Sakai, M. Takahashi and S. Shimada, *J. Cryst. Growth*, **312**, 2823–2827 (2010).
72) M. He, P. Zhou, S. N. Mohammad, G. L. Harris, J. B. Halpern, R. Jacobs, W. L. Sarney and L. Salamanca-Riba, *J. Cryst. Growth*, **231**, 357–365 (2001).
73) A. M. S. ElAhl, M. He, P. Zhou, G. L. Harris, L. Salamanca-Riba, F. Felt, H. C. Shaw, A. Sharma, M. Jah, D. Lakins, T. Steiner and S. N. Mohammad, *J. Appl. Phys.*, **94**, 7749–7756 (2003).
74) M. Toth, K. Fleischer and M. R. Phillips, *Phys. Rev. B*, **59**, 1575–1578 (1999).
75) M. A. Reshchikova and H. Morkoc, *J. Appl. Phys.*, **97**, 061301 (2005).
76) H. H. Tippins, *Phys. Rev.*, **140**, A316–A319 (1965).
77) E. G. Villora, T. Atou, T. Sekiguchi, T. Sugaware, M. Kikuchi and T. Fukuda, *Solid State Commun.*, **120**, 455–458 (2001).
78) C. H. Qiu and J. I. Pankove, *Appl. Phys. Lett.*, **70**, 1983–1985 (1997).
79) T. Y. Lin, H. C. Yang and Y. F. Chen, *J. Appl. Phys.*, **87**, 3404–3408 (2000).
80) N. Guo, H. You, Y. Song, M. Yang, K. Liu, Y. Zheng, Y. Huang and H. Zhang, *J. Mater. Chem.*, **20**, 9061–9067 (2010).
81) B. Lei, L. Sha, H. Zhang, Y. Liu, S. Man and S. Yue, *Solid State Sci.*, **12**, 2177–2181 (2010).
82) S. Kikkawa, N. Hatta and T. Takeda, *J. Am. Ceram. Soc.*, **91**, 924–928 (2008).
83) Y. Masubuchi, T. Hata, T. Motohashi and S. Kikkawa, *J. Solid State Chem.*, **184**, 2533–2537 (2011).
84) P. Dorenbos, *J. Lumin.*, **104**, 239–260 (2003).
85) W. Klemm and G. Winkelmann, *Z. Anorg. Allg. Chem.*, **288**, 87–90 (1956).
86) W. C. Koehler and E. O. Wollen, *Acta Crystallogr.*, **6**, 741–742 (1953).

Yuji Masubuchi received the Ph. D. degree in Engineering from Hokkaido University in 2005. From 2005 to 2007, he was a Technical Researcher in Technical Research Laboratory of Nippon Sheet Glass (NSG). He is currently an Assistant Professor from 2007 in Faculty of Engineering, Hokkaido University, Japan. His current research interests include synthesis, crystal structure and properties of novel functional oxynitride ceramics.